Research Article

Stingrays in the radio sky: Two unusual diffuse radio relic sources in the direction of the Magellanic Stream

Zachary J. Smeaton[1], Miroslav D. Filipović[1], Bärbel S. Koribalski[1,2], Manami Sasaki[3], Rami Z. E. Alsaberi[1,4], Aaron C. Bradley[1], Evan J. Crawford[1], Shi Dai[1,2], Nikhel Gupta[5], Frank Haberl[6], Andrew M. Hopkins[7], Thomas H. Jarrett[1,8,†], Sanja Lazarević[1,2,9], Denis Leahy[10], Peter Macgregor[1,2], Gavin Rowell[11], Stanislav S. Shabala[12], Dejan Urošević[13], Jacco Th. van Loon[14] and Tessa Vernstrom[5,15]

[1]Western Sydney University, Penrith South DC, NSW 2751, Australia, [2]Australia Telescope National Facility, CSIRO, Space and Astronomy, Epping, NSW, Australia, [3]Dr Karl Remeis Observatory, ErlangenCentre forAstroparticle Physics, Friedrich-Alexander-Universität Erlangen-Nürnberg, Bamberg, Germany, [4]Faculty of Engineering, Gifu University, Gifu, Japan, [5]Australia Telescope National Facility, CSIRO, Space and Astronomy, Bentley,WA, Australia, [6]Max-Planck-Institut für extraterrestrische Physik, Gießenbachstraße, Garching, Germany, [7]School of Mathematical and Physical Sciences, 12Wally'sWalk, Macquarie University, Sydney, NSW, Australia, [8]Department of Astronomy, University of Cape Town, Rondebosch, South Africa, [9]Astronomical Observatory, Belgrade, Serbia, [10]Department of Physics and Astronomy, University of Calgary, Calgary, AB, Canada, [11]School of Physics, Chemistry and Earth Sciences, The University of Adelaide, Adelaide, Australia, [12]School of Natural Sciences, Private Bag 37, University of Tasmania, Hobart, TAS, Australia, [13]Department of Astronomy, Faculty of Mathematics, University of Belgrade, Belgrade, Serbia, [14]Lennard-Jones Laboratories, Keele University, Keele, UK and [15]International Centre for Radio Astronomy Research (ICRAR), The University of Western Australia, Perth, Australia

Abstract

We present the discovery of two extended, low surface-brightness radio continuum sources, each consisting of a near-circular body and an extended tail of emission, nicknamed Stingray 1 (ASKAP J0129–5350) and Stingray 2 (ASKAP J0245–5642). Both are found in the direction of the Magellanic Stream (MS) and were discovered in the Australian Square Kilometre Array Pathfinder (ASKAP) Evolutionary Map of the Universe (EMU) survey at 944 MHz. We combine the ASKAP data with low-frequency radio observations from the GaLactic and Extragalactic All-sky MWA Survey (GLEAM) to conduct a radio continuum analysis. galaxy pairs or groups, and Odd Radio Circles (ORCs). We explore both Galactic/near Galactic scenarios, including runaway or circumgalactic supernova remnants (SNRs) and parentless pulsar-wind nebulae (PWNe), and extragalactic scenarios including radio active galactic nuclei (AGNs), dying radio galaxies, galaxy clusters, galaxy pairs or groups, head-tail radio galaxies, and ORCs, as well as the possibility that the morphology is due to a chance alignment. The Stingrays exhibit non-thermal emission with spectral indices of $\alpha = -0.89 \pm 0.09$ for Stingray 1 and $\alpha = -1.77 \pm 0.06$ for Stingray 2. We find that none of the proposed scenarios can explain all of the observed properties, however we determine it most likely that their shape is caused by some kind of complex environmental interaction. The most likely scenario from the available data is that of a head-tail radio galaxy, but more data is required for a definitive classification.

Keywords: Galaxies: Magellanic Clouds; radio continuum: general; ISM: supernova remnants; galaxies: active; galaxies: clusters: general

1. Introduction

The Evolutionary Map of the Universe (EMU) (Norris et al. 2011, 2021a; Hopkins et al. 2025, AS201) project is a large-scale radio survey conducted with the Australian Square Kilometre Array Pathfinder (ASKAP). ASKAP's modern phased array feed technology allows it to achieve an instantaneous field of view of ∼30 deg² enabling wide-field imaging surveys (Johnston et al. 2008; Hotan et al. 2021). By using the complete array of 36 ASKAP antennas,

EMU is currently imaging the entire southern sky with better sensitivity (∼30 μJy beam⁻¹) and resolution (15″) than previous all-sky surveys.

The EMU survey is currently ongoing, and its improved sensitivity has helped to reveal new low radio surface-brightness objects. A recent study by Ball et al. (2023) has shown ASKAP's ability to uncover a previously undiscovered population of low surface-brightness Galactic supernova remnants (SNRs), and this is also demonstrated by several other SNR and SNR candidate studies and discoveries (e.g. G278.92+1.35; Diprotodon; Filipović et al. 2024, G181.1−9.5; Kothes et al. 2017, G288.8−6.3; Ancora; Filipović et al. 2023; Burger-Scheidlin et al. 2024, G32.9−0.5; Perun; Smeaton et al. 2024b, G308.73+1.38; Raspberry; Lazarević et al. 2024a, G312.65+2.87; Unicycle; Smeaton et al. 2024a; Teleios; Filipović et al. 2025), including the first circumgalactic SNR J0624−6948 (Filipović et al. 2022; Sasaki et al. 2025). Additionally, ASKAP was used to discover a new class
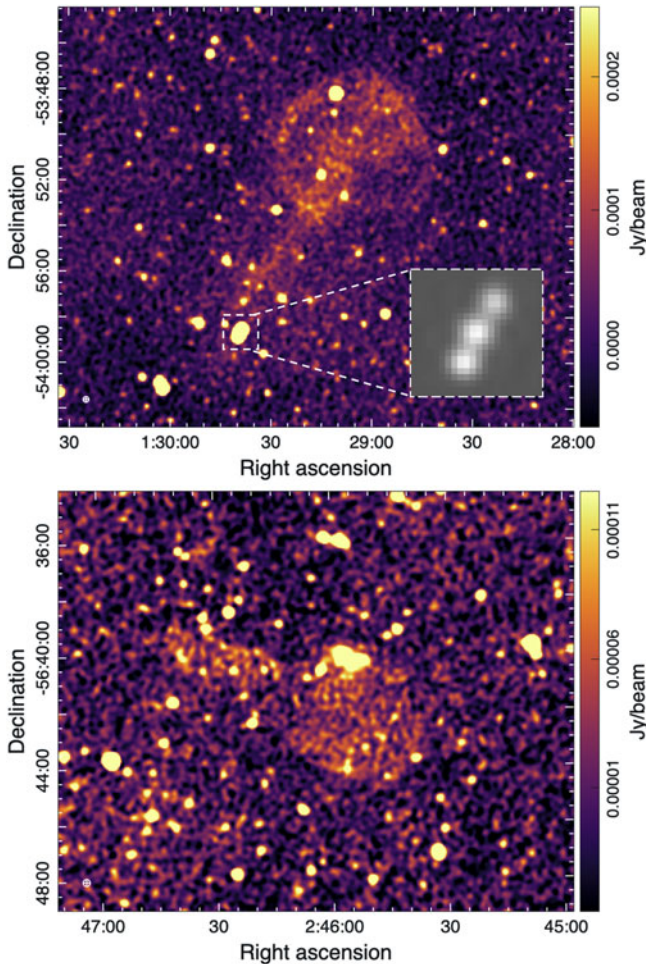
Figure 1. ASKAP EMU 944 MHz radio continuum images of two peculiar sources, named Stingray 1 (top) and Stingray 2 (bottom). Both images use linear scaling and have a restoring beam of 15″ which is shown in the bottom left corners. The Root Mean Squared RMS noise sensitivities are $\sigma = 25\,\mu$Jy beam^{-1} for Stingray 1 and $\sigma = 30\,\mu$Jy beam^{-1} for Stingray 2. The inset image in Stingray 1 shows the high-resolution (7″.7 × 7″.0) Australian Square Kilometre Array Pathfinder (ASKAP) image of the double-lobed radio galaxy associated with the galaxy WISEA J012939.26–535841.0 (see Section 4.2.1).

of low surface-brightness radio sources known as Odd Radio Circles (ORCs) whose nature and origin is still under investigation (Norris et al. 2021b; Koribalski et al. 2021; Norris et al. 2022). Also, using ASKAP, we found a very unusual active galactic nucleus (AGN) with recollimated jets in nearby NGC 2663 (Velović et al. 2022) as well as peculiar galaxy pair PKS 2130-538 within Abell 3785 cluster (Velović et al. 2023). ASKAP's sensitivity was also able to uncover some unusual faint, filamentary structures in the Abell S1136 galaxy cluster (Macgregor et al. 2024).

In this paper, we add to this list of interesting ASKAP discoveries two low surface-brightness diffuse radio sources. We nickname these objects 'Stingrays' due to their unusual head-tail radio shape (see Figure 1) resembling the animal. Another interesting feature is the Stingray's location in the direction of the Magellanic Stream (MS) which consists of H I gas that trails behind the Magellanic Clouds (MCs), a pair of nearby interacting dwarf galaxies. The origin of the MS is a topic of active investigation (Lucchini, D'Onghia, & Fox 2021; Wang, Hammer, & Yang 2022; Chandra et al. 2023; Lucchini, D'Onghia, & Fox 2024).

We conduct a radio continuum analysis using the available data to attempt to identify the nature of the Stingrays. We investigate

multiple possibilities, such as runaway SNRs within the MS, circumgalactic SNRs, pulsar-wind nebulae (PWNe), as well as further extragalactic scenarios such as radio AGNs, dying radio galaxies, galaxy clusters, galaxy pairs or groups, head-tail radio galaxies, and ORCs, as well as the possibility of a chance alignment of the different morphological components.

The paper is structured as follows; our observations and data are discussed in Section 2, analysis methods and results are in Section 3, a broad theoretical discussion is in Section 4, and our conclusions are in Section 5.

2. Observations and data reduction

This study primarily uses radio continuum data from the ASKAP EMU sky survey and the GaLactic and Extragalactic All-sky MWA Survey (GLEAM) as well as H I data from the HI4PI survey. See Table 1 for a summary of the observational properties. We searched for corresponding diffuse emission at multiple other frequencies, outlined in Section 3. The primary image analysis software used was the Cube Analysis and Rendering Tool for Astronomy (CARTA) (Comrie et al. 2021).

2.1. ASKAP

2.1.1. EMU

The areas of sky where the two Stingrays are located were observed as part of the large-scale EMU project (Hopkins et al. 2025; Norris et al. 2011, 2021a) (AS201) using the complete set of 36 ASKAP antennas at a central frequency of 943.5 MHz and a bandwidth of 288 MHz. Stingray 1 (ASKAP J0129–5350, Figure 1 top) was observed during two different scheduling blocks, SB50048 and SB60320, while Stingray 2 (ASKAP J0245–5642, Figure 1 bottom) was observed in SB49990. The total integration times are 20 h for Stingray 1 and 10 h for Stingray 2. The data were processed using the standard ASKAPsoft pipeline, including multi-scale cleaning, self-calibration, and multi-frequency synthesis imaging (Guzman et al. 2019). The images were downloaded from the CSIRO ASKAP Science Data Archive (CASDA).[a]

The ASKAP EMU data consists of Stokes I and V images. There is no detection in Stokes V, and so only the Stokes I images are used in our analysis. We use both the convolved and high-resolution Stokes I images which are produced by the standard ASKAPsoft pipeline (Guzman et al. 2019). Both these images are generated from the same calibrated dataset but have different imaging parameters applied. The high-resolution images are made using uniform weighting, resulting in beam sizes of typically ∼7″–9″ and increased noise. The convolved images are made using robust = 0 weighting and are restored using a 15″ beam. Further technical details can be found in Hopkins et al. (2025). The convolved images are the recommended science data products as they allow for accurate flux density measurements over the entire EMU survey.

We therefore use the convolved radio continuum images, shown in Figure 1, for any quantitative measurements such as flux density estimates, and hereafter the EMU image will refer to the 944 MHz convolved image unless otherwise stated. Since Stingray 1 is found in two different observations, these images were combined with the IMCOMB function in the Multichannel Image Reconstruction, Image Analysis and Display (MIRIAD)

Table 1. Details of the main radio continuum observations used in this work.

Telescope	Project	Observing date	Frequency (MHz)	Beam size (arcsec)	Pixel size (arcsec)	RMS
MWA	GLEAM	9 Aug 2013–18 Jun 2014	88	303×296 (S1)	24	∼50
				308×297 (S2)		
			118	222×216 (S1)		∼30
				222×216 (S2)		∼25
			155	173×167 (S1)		∼15
				170×163 (S2)		∼12
			200	145×138 (S1)		∼5
				143×134 (S2)		∼3
ASKAP	EMU	17 May 2023 and 22 Mar 2024 (S1)	944	15	2	0.025
	EMU	17 May 2023 (S1)	944	7.7 × 7.0	2	0.055
	EMU	13 May 2023 (S2)	944	15	2	0.030
	WALLABY	21 Oct 2024 and 29 Oct 2024 (S1)	1368	∼8	2	0.035
	WALLABY	21 Oct 2024 and 29 Oct 2024 (S1)	1368	15	2	0.025–0.030
Parkes	HI4PI	Jan 2005–Nov 2006 (GASS)	1420	974	300	43

Notes: The ASKAP observation dates are different for each object – we use (S1) for Stingray 1 and (S2) for Stingray 2 – and the Murchison Widefield Array (MWA) beam size and Root Mean Squared (RMS) are image-dependent. The HI4PI data is merged data from GASS and EBHIS. The Root Mean Squared RMS units are mJy beam^{-1} for all data except for HI4PI, which is mK.

software package (Sault, Teuben, & Wright 1995) using equal weighting. The resulting image is shown in Figure 1 (top); the RMS noise near Stingray 1 is 25 µJy beam^{-1}. The inset shows the high-resolution radio continuum image of the source WISEA J012939.26−535841.0 (see Section 4.2.1) with a synthesised beam of 7.″7 × 7.″0 and an RMS of $\sigma = 55$ µJy beam^{-1}. The bottom panel shows Stingray 2 in the convolved Stokes I image with a resolution of 15″ and an RMS of $\sigma = 30$ µJy beam^{-1}.

2.1.2. WALLABY

Stingray 1 is also detected in 1.4 GHz radio continuum images from the the Widefield ASKAP L-band Legacy All-sky Blind surveY (WALLABY) (AS202) (Koribalski et al. 2020; Westmeier et al. 2022), while the field containing Stingray 2 has not yet been observed. The central observing frequency for WALLABY is 1 367.5 MHz; due to RFI the bandwidth is limited to 144 MHz. Stingray 1 is detected in two separate scheduling blocks, SB67270 and SB66917, with a combined integration time of 16 h. The data is processed similar to the EMU data using the ASKAPsoft pipeline (Guzman et al. 2019), and the radio continuum images were downloaded from CASDA. Both images have angular resolutions of ∼8″ (8.3″×7.7″, P.A. = 74.9° for SB67270, and 8.2″×7.8″, P.A = 81.4° for SB66917) and were combined following the same process as for the EMU images. We measure an RMS noise sensitivity of ∼30−35 µJy beam^{-1} near Stingray 1. To increase sensitivity to diffuse emission, we convolve the the WALLABY image to 15″ resolution, matching that of the convolved EMU image. This convolved WALLABY image has an RMS noise sensitivity of ∼25−30 µJy beam^{-1} and is shown in the Appendix.

2.2. MWA

The sky region containing Stingrays 1 & 2 was also observed with the Murchison Widefield Array (MWA) telescope as part of the GLEAM survey (Wayth et al. 2015; Hurley-Walker et al. 2017; Hurley-Walker et al. 2019b, a). The data consists of four observations at the central frequencies of 88, 118, 155, and 200 MHz. The image bandwidth is 30 MHz, apart from the 200 MHz observations which have a bandwidth of 60 MHz. The size of the restoring beams and measured RMS noise levels are listed in Table 1.

2.3. HI4PI

We use HI spectral line data from the HI4PI survey, which consists of data from the Effelsberg-Bonn HI Survey (EBHIS) and the Parkes Galactic All-Sky Survey (GASS), as outlined in HI4PI Collaboration et al. (2016). Due to their location, the Stingrays are not observable by the Effelsberg telescope, but are covered by the Parkes telescope. The angular resolution is 16.′2 and the average RMS noise for the final data is 43 mK per channel with a channel width of 1.29 km s^{-1}.

3. Results

The Stingrays were discovered in the ASKAP EMU main survey when examining the 15″-resolution radio continuum images by eye while searching for interesting emission features. Following their discovery, we inspected images at multiple other frequencies, including infrared (*WISE* and *Spitzer*), optical (Sloan Digital Sky Survey (SDSS), SuperCOSMOS Hα Survey (SHS), and Dark Energy Camera Legacy Survey (DECaLS)), X-ray (eROSITA), as well as searching in γ-ray catalogues (*Fermi* 4FGL-DR4, Abdollahi et al. 2022). There are infrared, optical, and X-ray point sources that appear within the areas of the two Stingrays, however there is no diffuse emission at any other frequency that appears to correlate with the radio emission. Some of these point sources are investigated as potential host galaxies in Section 4.2.

Table 2. General morphological characteristics of the Stingrays including position, angular size (diameter for the circle region), and position angle (measured clockwise from North). The circle, tail, and total sections are defined by the regions outlined in Section 3.1.1.

Properties	Units	Stingray 1			Stingray 2		
		Circle	Tail	Total length	Circle	Tail	Total length
RA(J2000)	h:m:s	01:29:07.0	01:29:32.5	–	02:45:54.7	02:46:26.9	–
Dec(J2000)	d:m:s	–53:50:46.7	–53:56:34.7	–	–56:42:06.0	–56:40:15.2	–
Angular size	arcmin	7.0	6.8×1.6	13.8	4.8	4.8×1.2	9.6
Position angle	degr	–	150	–	–	76	–

3.1. Radio continuum

3.1.1. Morphology

We find two extended, very low surface-brightness radio sources with nearly matching, peculiar morphologies in the EMU data (see Figure 1). Each consists of a near-circular body and extended tail, spanning several arcminutes in size. Optical images of both sources show a number of possibly associated galaxies. Interestingly, both objects were found relatively close to each other and in the direction of the MS.

To determine the angular sizes of the Stingrays, we fit two regions around each Stingray using the astronomical imaging software CARTA. These regions are set by eye around the emission visible in the EMU images and consist of a circular and a tail region for each Stingray. The angular dimensions of these regions are given in Table 2. The total length of each Stingray is measured from the tip of the tail to the far side of the circle section (the far side being the edge of the circle opposite to the tail region). Overall, both Stingrays display a similar morphology with a circular head and extended tail, and Stingray 1 is ∼1.4 times larger than Stingray 2 in terms of total length.

There are several radio point sources within both Stingrays. We perform source finding using the AEGEAN[b] and Background and Noise Estimator (BANE) software of Hancock et al. (2012), Hancock et al. (2018), then cross-match them with the astronomical databases, SIMBAD[c] (Wenger et al. 2000) and NASA/IPAC Extragalactic Database (NED).[d] Most of the sources appear in these databases and some have redshifts. These sources, and the possibility of an association with the Stingrays, is discussed further in Section 4.2.

3.1.2. Flux density

We measure the flux density of the Stingrays with the imaging software CARTA using the regions as defined in Section 3.1.1 and Table 2. For the EMU images, the convolved images are used due to their self-consistent flux density measurements (see Section 2.1.1), and we remove the point sources using the Aegean Residual (AeReS) tool in the Aegean software package. AeReS was unable to properly remove the two brightest point sources and so these were subtracted manually to obtain flux densities both with and without point sources (Table 3). We refer to these flux densities throughout the text as the total flux density (total flux density from the regions including point sources), diffuse emission (total flux density from the regions once the point sources have been subtracted), and the point source flux density. For the WALLABY data, the signal-to-noise ratio is too low to be able to accurately measure any component other than the circular section's emission. We are unable to remove the point sources for the MWA images due to the lower resolution (Figure 2).

All images are then convolved to the largest beam (at 88 MHz) before flux extraction (the MWA 88 MHz image has a beam size of $303'' \times 296''$ for Stingray 1 and $308'' \times 297''$ for Stingray 2 and a pixel size of $24''$ for both; see Table 1) to ensure consistent scaling as described in Hurley-Walker et al. (2019a, Section 2.4). Errors are estimated as ∼10% following a similar process as Filipović et al. (2022).

3.1.3. Spectral index

SNRs have theoretical and observed average spectral index values of $\alpha = -0.5$ due to synchrotron emission from the acceleration of charged particles in their expanding shockwave (Bell 1978; Bozzetto et al. 2017, 2023; Cotton et al. 2024). For the MC SNR population, observational studies show a mean value of $\alpha \approx -0.5$, with a distribution range $-0.9 < \alpha < 0$ (Bozzetto et al. 2017; Maggi et al. 2019). Extragalactic radio sources typically have an average observed spectral index of $\alpha \sim -0.7$ to $\alpha \sim -0.8$, measured from independent large-scale radio studies (Condon 1984; Mauch et al. 2003; Pennock et al. 2021; Filipović et al. 2021), however the range of possible spectral indices is far wider and can extend from ultra-steep spectrum sources (Collier et al. 2014, 2018) to flat and inverted spectrum sources (Filipović et al. 2021; Balzan et al. 2022; Shobhana et al. 2023).

Total Spectral Index: We are able to separate the point source emission from the diffuse emission in the ASKAP images, however we are unable to do so in the GLEAM images due to the poorer resolution. As these are likely extragalactic radio sources with spectral indices ∼ –0.7 to –0.8, they may contribute significantly at lower frequencies and result in a significant overestimate of the GLEAM flux densities. Due to the similar observing frequencies between the EMU and the WALLABY data, it is not possible to accurately measure the spectral indices for many of the point sources within Stingray 1. We are unable to measure any point source spectral indices in Stingray 2 due to the lack of WALLABY data for this object. Therefore, we assume an average spectral index of $\alpha = -0.7$(Condon 1984; Filipović et al. 2021) for all radio point sources and use this to scale the fluxes to MWA frequencies. This ensures consistent methodology between the two Stingrays and reduces uncertainties. We use this spectral index to scale the 944 MHz EMU point source flux densities to MWA

Table 3. Measured flux densities of the Stingrays at all radio frequencies. All images were convolved to the lowest resolution for each object. For ASKAP, three flux measurements are given as described in Section 3.1.2: total (including point sources), diffuse (excluding point sources), and point sources (the difference of total and diffuse). Errors are taken as ∼10% with a minimum error of ± 1 mJy.

Telescope	ν	S_I (mJy)					
		Stingray 1					
	(MHz)	Circle			Tail		
MWA	88	439±44			358±36		
	118	298±30			253±25		
	155	208±21			180±18		
	200	205±21			143±14		
ASKAP		Total	Diffuse	Point sources	Total	Diffuse	Point sources
	944	54±5	36±4	18±9	52±5	23±2	29±7
	1368	31±3	17±2	14±5	–	–	–
		Stingray 2					
		Circle			Tail		
MWA	88	156±16			273±27		
	118	90±9			178±18		
	155	52±5			105±11		
	200	39±4			55±6		
ASKAP	944	Total	Diffuse	Point sources	Total	Diffuse	Point sources
		7±1	4±1	3±2	5±1	2±1	3±2
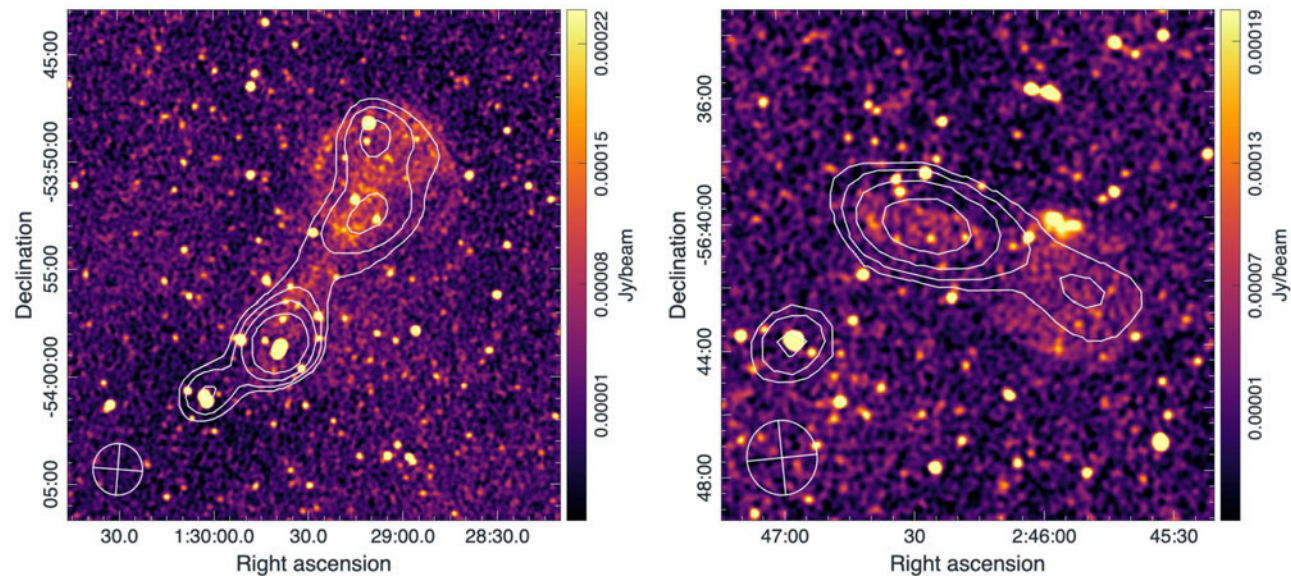
Figure 2. ASKAP EMU 944 MHz radio continuum images of Stingray 1 (left) and Stingray 2 (right) overlaid with GLEAM 200 MHz contours. Both images use linear scaling. The background image is the same EMU image as shown in Figure 1. The contours are from the 200 MHz MWA image with a restoring beam of 145″×138″ and RMS noise sensitivity of $\sigma = 4.5$ mJy beam^{-1} for Stingray 1 (left), and a restoring beam of 143″×134″ and RMS noise sensitivity of $\sigma = 3.0$ mJy beam^{-1} for Stingray 2 (right) (see Table 1). Contour levels are at ∼5, 7, 10, and 15 σ for each image and the MWA beam sizes are shown in the bottom left corners.

frequencies ('Scaled' column in Table 4). We then subtract this scaled flux density from the total measured flux density (MWA rows in Table 3) to estimate the diffuse flux density for the circle and tail regions at MWA frequencies ('Diffuse' columns in Table 4). Errors are estimated as ∼10% following our method for measured fluxes in Section 3.1.2.

We plot the estimated flux density from the diffuse emission against the observing frequencies to obtain a spectral index value

Table 4. Calculated scaled and diffuse flux densities of the Stingrays assuming a spectral index $\alpha = -0.7$ for extragalactic point sources. Scaled flux densities are the sum of the point source flux densities measured from the EMU data (Table 3 'Point sources' column) scaled to MWA frequencies using the assumed spectral index $\alpha = -0.7$. Diffuse flux densities are the difference between the total MWA flux densities from Table 3 and the scaled point source flux densities. Errors are taken as ~10%. The spectral index values calculated using these scaled fluxes and the fluxes from Table 3 are shown in the bottom two rows.

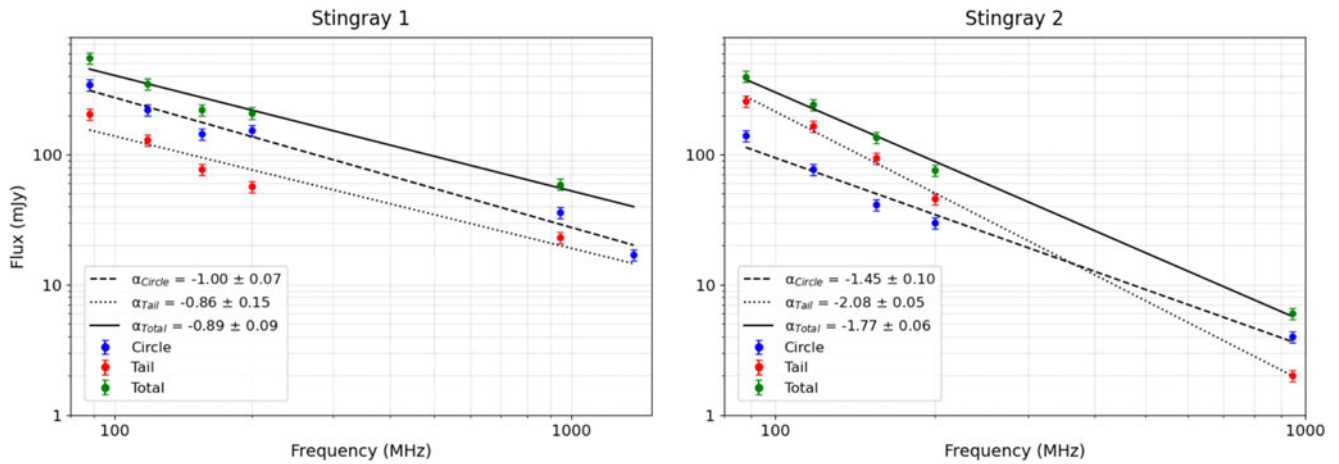|	S_I (mJy)							
ν	Stingray 1				Stingray 2			
	Circle		Tail		Circle		Tail	
(MHz)	Scaled	Diffuse	Scaled	Diffuse	Scaled	Diffuse	Scaled	Diffuse
88	95±10	344±34	153±15	205±21	16±2	140±14	16±2	257±26
118	77±8	221±22	124±12	129±13	13±1	77±8	13±1	165±17
155	64±6	144±14	103±10	77±8	11±1	41±4	11±1	94±9
200	53±5	152±15	86±9	57±6	9±1	30±3	9±1	46±5
α	-1.00 ± 0.07		-0.86 ± 0.15		-1.45 ± 0.10		-2.08 ± 0.05	
		-0.89 ± 0.09				-1.77 ± 0.06		

Figure 3. Spectral index components for each Stingray. The different colours and line styles represent the different regions. Flux density values used are the diffuse values from Tables 3 and 4. The line of best fit is calculated using the linear least-squares regression method.

for each object (Figure 3). We use the diffuse flux density measurements as described in Section 3.1.2 (the 'Diffuse' columns in Table 3) for the circular and tail regions. For the MWA data the diffuse flux density used ('Diffuse' column in Table 4) is estimated as the total measured flux density (MWA rows in Table 3) minus the scaled point source contribution ('Scaled' columns in Table 4). The WALLABY data is only used for the circle region of Stingray 1 as the tail region could not be reliably measured. These diffuse flux densities are used to fit the spectral indices for the circle and tail components (α_{Circle} and α_{Tail} in Figure 3). The circle and tail diffuse flux densities are then summed together to calculate the total diffuse flux density for the entire area of each Stingray at each frequency (excluding the WALLABY 1 368 MHz data point as the tail flux density could not be measured). When we defined the regions in Section 3.1.1, we ensured that the circle and tail regions were adjacent regions but not overlapping, thus summing these flux densities together does not measure any emission twice. These total flux density values for the diffuse emission are then used to calculate the spectral index of the whole object (α_{Total} in Figure 3).

The spectral indices were calculated from the slope of the line of best fit through the data points, which is calculated using the LINREGRESS[e] function in the Python SCIPY package (Virtanen et al. 2020). This method applies a linear least-squares regression method to the data to find the line of best fit, and the quoted uncertainty is the standard error of the fit (Theil 1950). The plotted spectral indices are shown in Figure 3 and the calculated final values are shown in Table 4.

We note that the quoted spectral index uncertainties are the statistical uncertainties, and this method of estimating extragalactic spectral indices could introduce additional uncertainties into this method which are not reflected in the standard error. This uncertainty can be seen in the fit of some of the data points, such as the tail section of Stingray 1 (Figure 3, left), which shows deviation from the linear fit. This uncertainty is most pronounced in the Stingray 1 tail, most likely due to this section having more point source contribution than the other areas. Thus, the flux density
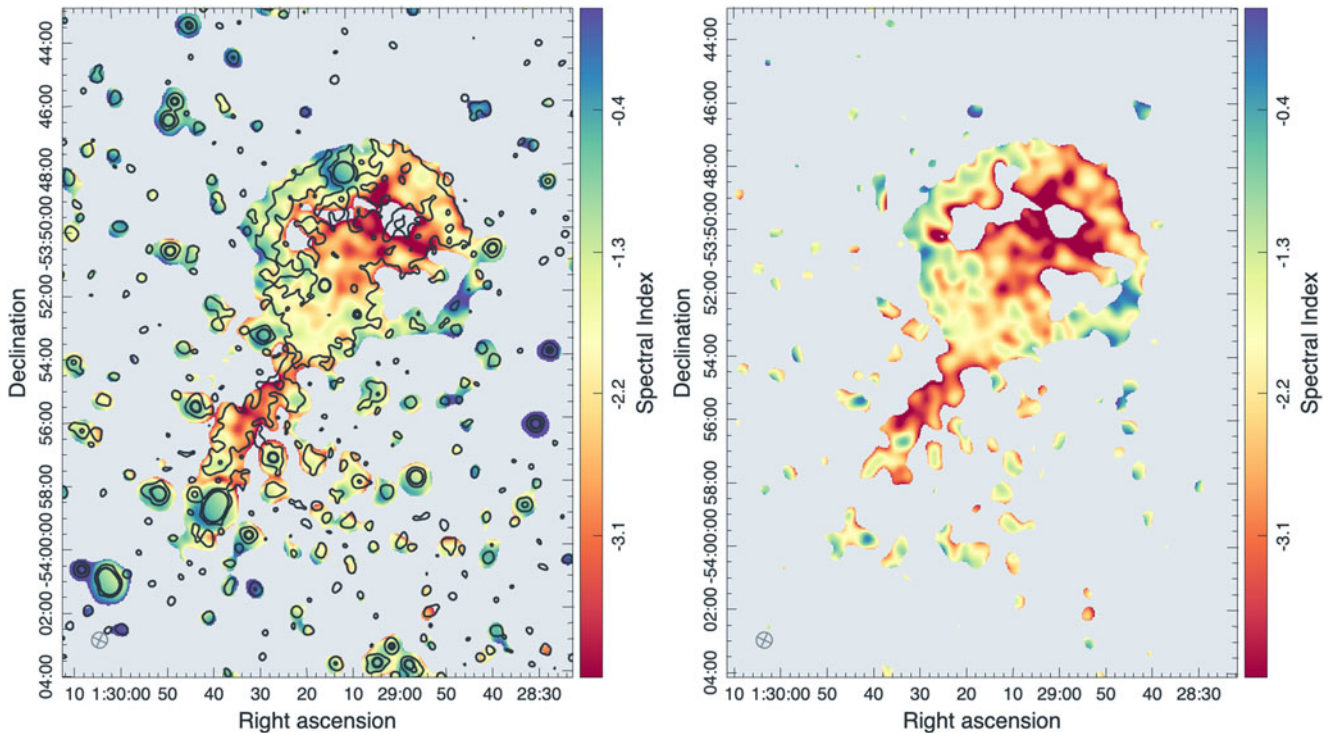
[e]https://docs.scipy.org/doc/scipy/reference/generated/scipy.stats.linregress.html.

Figure 4. Spectral index maps of Stingray 1 derived from ASKAP images at 944 and 1 368 MHz after each was smoothed to a resolution of 30″. The resolution is shown in the bottom left corner of each image. Left: Spectral index with point sources included. Black contours are from 944 MHz ASKAP images at levels of 60, 300, and 400 μJy beam^{-1}. Right: Spectral index map of the diffuse emission component after point source subtraction using AeReS. The two largest point sources were manually masked before image generation.

scaling assumption has more impact here, and this may cause deviation from a linear fit.

As this method relies on assuming a spectral index of $\alpha = -0.7$ for the radio point sources, it is possible that this value overestimates the steepness of the derived spectral indices. While some extragalactic radio sources can have significantly steeper spectral indices (e.g. ultra-steep spectrum sources), this would result in an overestimation of the point source contribution at MWA frequencies and the spectral indices may be flatter.

This method assumes a spectral index which is scaled to MWA frequencies and removed, introducing some uncertainty to the measurements. This is particularly relevant for the source WISEA J012939.26-535841.0 located at the tip of tail of Stingray 1. At MWA frequencies, this source begins to dominate and we are unable to separate the diffuse tail emission. This source is also catalogued as the GLEAM source J012938−535829 with a measured spectral index of $\alpha = -1.24 \pm 0.07$ (Hurley-Walker et al. 2017) using the GLEAM bands. Due to the larger beam size, these MWA measurements are likely contaminated by the diffuse tail and thus cannot be used to separate the emission. These uncertainties make it difficult to determine exact values for the spectral indices; however, the different methods applied all give relatively steep spectral indices, indicating that the Stingrays are overall non-thermal emitters with $\alpha \lesssim -0.8$. Additionally, the circular area of Stingray 1 and the tail area of Stingray 2 have been catalogued as GLEAM sources GLEAM J012911−535238 with $\alpha = -1.32 \pm 0.13$ and GLEAM J024626−564007 with $\alpha = -1.86 \pm 0.10$ (Hurley-Walker et al. 2017). These values are solely from the MWA bands, but provide further evidence for the Stingrays's non-thermal nature.

Spectral Index Map: We also generate a spectral index map using the ASKAP EMU and WALLABY data for Stingray 1 (Figure 4). We are only able to generate a spectral index map for Stingray 1, as there is not yet WALLABY data available for Stingray 2 and so we do not have sufficiently high-resolution radio data at multiple frequencies to resolve the Stingray 2 spectral index structure adequately. The total spectral index map including point sources is shown on the left, and only the diffuse component is shown on the right. To map the diffuse component, the point sources were removed using AeReS as described in Section 3.1.2 and the two largest point sources were manually masked. Both ASKAP images were convolved to a common resolution of 30″ before the spectral index map generation. The map was generated using the MATHS function from the MIRIAD software package (Sault et al. 1995). As we are calculating the spectral index value from only two datasets, we are able to do it with a simple equation where we calculate α as the linear slope between two data points: $\alpha = (\log(S_{\mathrm{WALLABY}}) - \log(S_{\mathrm{EMU}}))/(\log(1367) - \log(944))$, where S are the pixel values measured from the WALLABY and EMU images respectively. The MATHS function generates this spectral index value for each pixel in the ASKAP images to generate the spectral index map. The cuts were selected at the highest contour level that showed the full extent of Stingray 1 in the convolved images so as to reduce background contamination. Figure 4 (left) has the 944 MHz ASKAP radio contours overlaid to show the Stingray's extent. The point sources present in this image predominantly show values $\alpha \sim -0.7$, providing justification for our earlier assumption.

Figure 4 (right) shows a steep spectral index for Stingray 1, with a circle average of $\sim$−2.4 and a tail average of $\sim$−2.8. This is

Table 5. Calculated radio surface brightness for each Stingray. Area is calculated from regions defined in Section 3.1.1 and flux density is scaled to $\nu = 1$ GHz using spectral indices from Table 4.

	Ω	$S_{1\,\text{GHz}}$	$\Sigma_{1\,\text{GHz}}$
	$(\times 10^{-6}$ sr$)$	(mJy)	$(\times 10^{-23}$ W m^{-2} Hz$^{-1})$
Stingray 1	4.0	524	13.1
Stingray 2	1.9	5.2	2.7

steeper than the estimated values from Figure 3 where the MWA scaled fluxes were also accounted for. This is not unexpected as Stingray 1 is difficult to accurately measure in the WALLABY images due to the lower sensitivity, shorter observation time, smaller bandwidth, and the intrinsically lower flux density at the higher frequency. There is also possibly a significant error in both estimation methods, due to the scaling of the MWA point source flux densities, and due to calculating the spectral index from only two frequency measurements. Despite these uncertainties however, it is clear that Stingray 1 appears as a steep spectrum source, likely indicating an evolved object, as discussed in Section 4.

3.1.4. Surface brightness

The surface brightness is a measure of how bright the radio emission is per unit of angular area of the source. The relationship is given as $\Sigma_{1\text{GHz}} = S_{1\text{GHz}}/\Omega$, where $\Sigma_{1\text{GHz}} =$ surface brightness at 1 GHz, $S_{1\text{GHz}} =$ flux density at 1 GHz, and $\Omega =$ angular area of object (Filipović & Tothill 2021). We use the measured spectral indices from Table 4 to calculate the scaled flux at $\nu = 1$ GHz and calculate the area of the source from the regions described in Section 3.1.1. We use these values to calculate the radio surface brightness of the Stingrays (Table 5).

These are particularly low surface-brightness values and the causes for this differ for each origin scenario discussed. More detail is given for each possible origin scenario in Section 4. This lower value could also indicate expansion into an extremely rarefied environment, and this scenario would also help explain the observed symmetry in the circular region. For extragalactic sources, such a low surface brightness may be caused by redshift dimming. This is an effect where sources at higher redshifts experience dimming in their surface brightness due to their large distance (Calvi et al. 2014).

3.2. H I analysis

A commonly used method to determine distances to celestial objects is that of H I absorption. There are regions of H I gas and dust throughout the Universe, and these clouds absorb and emit light at specific wavelengths as the light travels through it. This absorption occurs at a specific redshift depending on the object's velocity, which can be attributed to a specific distance from us. These absorption dips can be seen in an object's H I spectrum, and by measuring the velocity of the absorption dips, the distance to the objects can be constrained. A good theoretical review is given in Leahy & Tian (2010), and this H I absorption method has been used extensively for both Galactic and extragalactic sources (e.g. Koribalski et al. 1995; Leahy & Tian 2012; Zhang et al. 2021).

By measuring absorption in an object's H I spectrum, we can determine if an object is located in front of or behind these H I clouds, allowing us to constrain the distance if the cloud distance
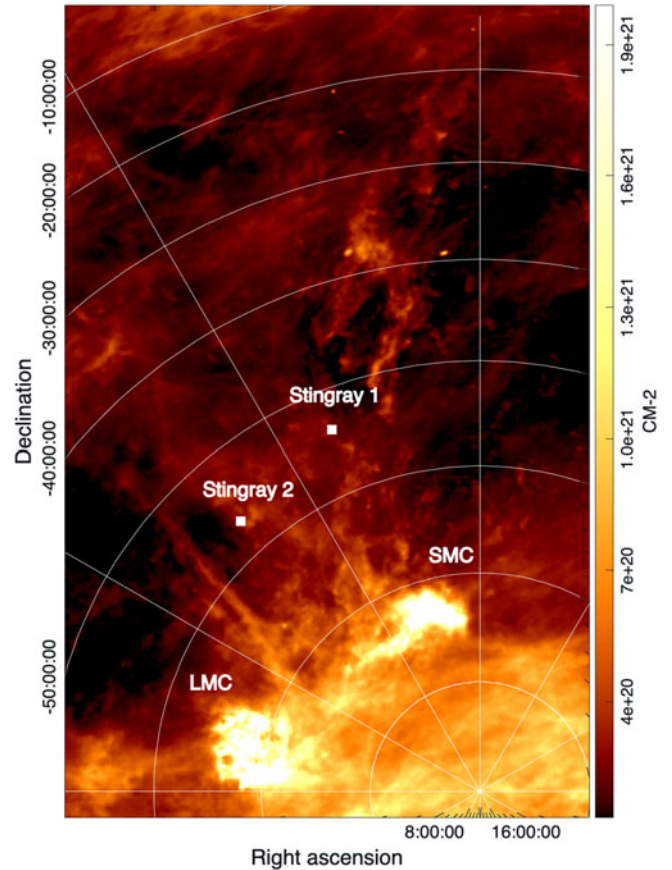

Figure 5. Total H I column density map of the Magellanic System using data from the Parkes Galactic All-Sky Survey (GASS, HI4PI Collaboration et al. 2016). The locations of the LMC and SMC as well as Stingrays 1 and 2 are annotated. The Magellanic Stream extends north (upward) of the SMC and consists of several H I filaments and diffuse emission.

is known. Several surveys have been conducted to determine the geometry, velocity, and H I gas distribution within the MS (Haynes 1979; Putman 2000; Bland-Hawthorn & Putman 2001; Putman et al. 2003; Brüns et al. 2005). The MS is typically split up into 4 sections with differing velocities. We compare the locations of the Stingrays with the H I map of Putman (2000), their Figure 2 and determine both Stingrays are located in Section MS I (Figure 5). This region represents the positive velocity section that are above Galactic velocities, that is 30 km s^{-1} < V_{LSR} < 250 km s^{-1}. We should also see absorption from Galactic H I, and these velocities correspond with –40 km s^{-1} < V_{LSR} < 30 km s^{-1} (Brüns et al. 2005).

We measure the H I absorption spectrum for the Stingrays (Figure 6) using data from the HI4PI survey (Section 2.3) using the same total region as defined in Section 3.1.1 and Table 2. Both show absorption dips at the expected velocities of the Milky Way and MS (Figure 6 and Table 6).

We select an area that is stable with no obvious dips in both spectra as an estimate of the background noise levels. Taking this region as $-400 \leq V_{\text{LSR}} \leq -100$ km s^{-1} we measure the standard deviations and the signal-to-noise ratio of our peaks (Table 6). We measure background noise levels of 0.05 for Stingray 1 and 0.08 for Stingray 2. The background noise level for Stingray 2 is ∼1.5 times that of Stingray 1. This could be caused by difficulties isolating the diffuse emission from the background due to the significantly

Table 6. Results from H I absorption analysis. σ is calculated from the background region, taken as $-400 \leq V_{LSR} \leq -100$ km s^{-1}.

	σ	Milky Way peak			Magellanic Stream peak		
		V_{LSR} (km s^{-1})	$e^{-\tau}$	Signal-to-noise	V_{LSR} (km s^{-1})	$e^{-\tau}$	Signal-to-noise
Stingray 1	0.05	−7.6	0.6	8.3	195.9	0.8	3.8
Stingray 2	0.08	−6.3	0.5	7.0	168.9	0.2	9.8
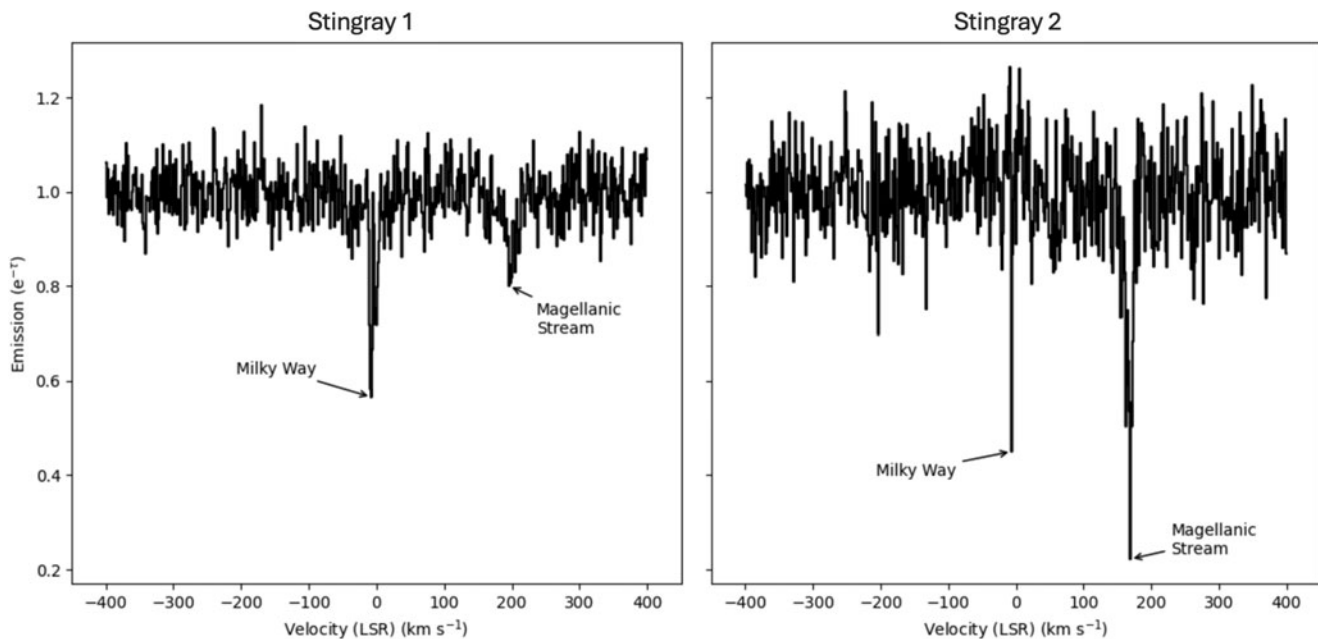
Figure 6. H I absorption spectrum for each Stingray from HI4PI data. The absorption dips for both the Milky Way and Magellanic Stream are annotated.

lower surface brightness (Table 5). Despite the higher background noise, we still obtain a spectrum with clear absorption dips.

Both Stingrays show observable dips at MilkyWay (MW) and MS velocities. Stingray 1 shows a MW peak at $V_{LSR} = -7.6$ km s^{-1} with a value $e^{-\tau} = 0.6$ at a 8.3σ detection level, and a MS peak at $V_{LSR} = 195.9$ km s^{-1} with a value $e^{-\tau} = 0.8$ at a 3.8σ detection level. Stingray 2 shows a MW peak at $V_{LSR} = -6.3$ km s^{-1} with a value $e^{-\tau} = 0.5$ at a 7.0σ detection level and a MS peak at $V_{LSR} = 168.9$ km s^{-1} with a value $e^{-\tau} = 0.2$ at a 9.8σ detection level.

We take any point above a 5σ detection to be a real detection and any point above 3σ to be a probable detection. As expected, both Stingrays show real absorption dips for the Milky Way. We also detect a real absorption dip for Stingray 2 for the MS, and a probable dip for Stingray 1 corresponding with the MS velocities. This analysis shows that both Stingrays are located beyond the MW as we clearly detect absorption due to the MW H I. Stingray 2 also shows clear absorption in H I at the MS velocities, indicating that Stingray 2 is located behind the MS. Stingray 1 shows a probable absorption at MS velocities, indicating that it is likely located behind the MS, but the detection is not conclusive.

4. Discussion

We investigate two main origin scenarios of the Stingrays, the first being that of a Galactic, or near Galactic, source, where the origin scenarios discussed are a supernova remnant (SNR) from a runaway star(s) within the MS (see Section 4.1.1), a circumgalactic SNR on the outskirts of the MW or MS (see Section 4.1.4), and a Galactic pulsar-wind nebula (PWN) (see Section 4.1.5). The second origin scenario is that of a distant extragalactic source where the origin scenarios discussed are radio active galactic nuclei (AGN) (see Section 4.2.1), dying radio galaxies (see Section 4.2.2), galaxy clusters (see Section 4.2.3), galaxy pairs/groups (see Section 4.2.4), head-tail radio galaxies (see Section 4.2.5), and Odd Radio Circles (ORCs) (see Section 4.2.6).

4.1. Origin: Galactic/near Galactic

It is possible that the Stingrays are associated with the MS or that they are Galactic objects. We consider both scenarios here; specifically runaway SNRs from the MCs, circumgalactic SNRs located on the outskirts of the MCs or MW, and Galactic PWNe. We also discuss the likelihood of the Stingrays being associated with the MS.

4.1.1. Runaway SNRs

One possible explanation for the unusual morphology of the Stingrays is that they are SNRs from runaway stars. Runaway stars are stars that have been ejected from their parent cluster, typically with high velocities. There are two main mechanisms that cause this stellar ejection; the ejection by gravitational interactions in

dense star clusters, or when a star in a binary system undergoes a supernova (SN) explosion ejecting its companion (Blaauw 1961; Filipović et al. 2022). Runaway stars have been detected from both the Large Magellanic Cloud (LMC) and Small Magellanic Cloud (SMC), and several are confirmed to be massive enough to explode as Type II SN (Gvaramadze, Pflamm-Altenburg, & Kroupa 2011; Lin et al. 2023). Hydrodynamic models have predicted that these runaway SN may form asymmetric and unusual SNR morphologies (Velázquez et al. 2006; Meyer et al. 2015; Filipović et al. 2022). This scenario could explain the unusual observed morphology and identification of SNRs within the MS would help to further classify the MS stellar population.

4.1.2. Association with Magellanic Stream

Our H I analysis shows a real Milky Way absorption dip for both Stingrays (signal-to-noise ratios: 8.3 for Stingray 1 and 7.0 for Stingray 2), a real MS dip for Stingray 2 (signal-to-noise ratio: 9.8) and a probable MS dip for Stingray 1 (signal-to-noise ratio: 3.8). This indicates that we are seeing absorption from the MW H I for both Stingrays's emission indicating they are located outside of the Milky Way, and that we are seeing absorption from the MS H I for Stingray 2, indicating that Stingray 2 is also located beyond the MS. The spectrum for Stingray 1 is less definitive. Since we see a dip of $> 3\sigma$ it is likely a real detection, and the lower absorption level may be due to the light travelling through a smaller amount of H I. The MS is not consistent in its H I column density (Brüns et al. 2005), and it may be that this direction contains less H I. This could be due to a lower H I density in this region, or the MS may be thinner in this direction so the emission is travelling through less material. It is also possible that Stingray 1 is located within the MS instead of on the far side, and so the emission is travelling through less H I. While it is difficult to discern between these possibilities without higher resolution H I data, we can say that it is unlikely that Stingray 1 is located in front of the MS as we are seeing a small amount of absorption at the MS velocity distance. We therefore conclude that Stingray 1 has a possible but unlikely association with the MS, and Stingray 2 has no physical association with the MS.

4.1.3. SNR spectral index

We compare the spectral indices of the Stingrays with those of the known LMC and SMC SNR population using the statistical analyses of Bozzetto et al. (2017), Zangrandi et al. (2024) for the LMC and Maggi et al. (2019), Cotton et al. (2024) for the SMC. Both analyses show similar distributions. The mean spectral index value is $\alpha \approx -0.5$, with a distribution range $-0.9 < \alpha < 0$.

We now compare our measured spectral indices (Tables 4 and 2) with the theoretical SNR average and the observed MC distribution range. Both Stingrays have steeper spectral indices than the theoretical value, $\alpha = -0.5$ (Bell 1978), as well as being outside of the MC SNR population. For Stingray 1, the spectral index, $\alpha = -0.89$, is on the extreme end of the distribution, and Stingray 2's spectral index, $\alpha = -1.77$, is far outside of the range entirely. This comparison, coupled with our H I analysis, makes it unlikely that they are SNRs associated with the MS.

It is possible that the Stingrays have flatter spectral indices than those estimated here, due to the inherent uncertainty in our scaling of the MWA flux densities. If the extragalactic point sources instead have a steeper spectral index than we assumed, this would mean that we underestimated the point source contribution at MWA frequencies, and thus the spectral indices may indeed fall within the MC SNR population range, although our H I analysis (Section 3.2) still indicates that the objects are located beyond the MS.

4.1.4. Circumgalactic SNRs

There is the possibility that the Stingrays may be circumgalactic SNRs. These are SNRs that are located on the outskirts or just outside of their host galaxy. Two such SNRs have been previously observed near the LMC, SNR J0624–6948 (Filipović et al. 2022; Sasaki et al. 2025) and SNR J0614–7251 (Sasaki et al. 2025), so it is possible that the Stingrays are members of the MC SNR population that have moved outside of the Galaxy.

The spectral index of the Stingrays ($\alpha = -0.89$ for Stingray 1 and $\alpha = -1.77$ for Stingray 2) is above the theoretical average of $\alpha = -0.5$ for SNRs. Stingray 2 is well outside of the MC SNR observed distribution ($-0.9 < \alpha < 0$) and Stingray 1 is just above the lower limit, making it unlikely that they are circumgalactic to the MS. While the spectral index steepness may have been over-estimated due to our assumptions about the MWA point source flux densities, it is still likely that they fall outside of the MC population, particularly in the case of Stingray 2, thus arguing against this classification.

The size of the Stingrays may present issues with this possibility as well. If we assume an average distance of ∼55 kpc to the MS (50 kpc for the LMC and 60 kpc for the SMC), then the Stingrays have approximate physical diameters of 110 pc (Stingray 1) and 80 pc (Stingray 2), considering only the circular region. These diameters are larger than expected for the typical LMC SNRs population, which Bozzetto et al. (2023) show to have mean diameters of 44.9 pc (S.D. = 24.9 pc), although there are a handful of known and candidate SNRs to have diameters >100 pc (Yew et al. 2021; Smeaton et al. 2025). This LMC distribution is similar to the statistical distributions of SMC SNRs (mean diameter = 48 pc (S.D. = 19 pc); Cotton et al. 2024), Galactic SNRs (mean diameter = 21.9±1.7 pc; Ranasinghe & Leahy 2023), and SNRs in other nearby galaxies (for example, M31 with a mean diameter = 44.2±1.5 pc; Ranasinghe & Leahy 2023; Galvin & Filipovic 2014). While this larger size does not exempt the Stingrays from classification as an SNR, the larger than expected size is evidence against this scenario, especially since this analysis only considers the size of the circle region, excluding the tail region.

4.1.5. Parentless Pulsar-Wind Nebula

Finally, we could also consider a PWN without an associated SNR scenario, such as Potoroo (Lazarević et al. 2024b), Lighthouse (Pavan et al. 2016; Pavan et al. 2014), or the Guitar nebula (Cordes, Romani, & Lundgren 1993). While the Stingrays appear morphologically similar, the spectral index for such a PWN is expected to be flat. This is in disagreement with what we find for the Stingrays, and so this scenario is deemed unlikely.

4.2. Origin: Extragalactic

Since our H I analysis shows it unlikely that the Stingrays are located in the MS or Galaxy, it is most likely that they are located on the same line of sight but in the background, far out from the Local Group. This is the second main scenario we investigate; that of distant extragalactic radio sources. The spectral index indicates non-thermal emission, and so we examine some classes of extragalactic objects that exhibit extended non-thermal radio emission;

that includes radio AGNs, dying radio galaxies, galaxy clusters, galaxy pairs/groups, head-tail radio galaxies, and ORCs. A prudent next step in this analysis is to identify any known galaxies that may be a host galaxy.

There are multiple galaxies that appear in the NED database within the region of the objects. For Stingray 1, we find 16 galaxies in the region of diffuse emission, and for Stingray 2 we find 11 galaxies. These galaxies are best seen in the optical, and we show their spatial correlation using optical data in the g, r, i, and z bands from the Dark Energy Spectroscopic Instrument (DESI) Legacy Survey DR10[f] (Dey et al. 2019) (Figure 7). We also search the available optical and infrared (IR) images by eye to identify the brightest of these galaxies for analysis in the following relevant sections.

4.2.1. Radio AGN

Extended non-thermal radio emission is observed in a fraction of AGNs ($\sim$10–20%), known as radio loud AGNs (Hardcastle & Croston 2020; Diana et al. 2022). These AGNs have highly energetic jets and lobes visible at radio frequencies due to charged particles emitted from the host galaxy's Super Massive Black Hole (SMBH). These jets can extend out to Mpc distances from the galaxy and form complex shapes (Blandford et al. 2019; Dabhade et al. 2020). Radio AGNs exhibit a diverse variety of complex shapes (e.g. Pedlar et al. 1990; Owen et al. 1985; O'Dea & Owen 1986; Velović et al. 2022, 2023).

The jets and lobes of radio AGN are caused by synchrotron emission from relativistic electrons and typically have steep spectral indices, $\alpha \sim -0.7$ to $\alpha \sim -1.0$, while the central core typically has a flat spectral index due to the constant energy input from the SMBH (Bridle & Perley 1984). There is also a subset of AGNs with steeper spectral indices (up to $\alpha = -1.6$), known as dying or remnant radio galaxies (Murgia et al. 2011; Brienza et al. 2016). The spectral indices of the Stingrays fall within these ranges, with Stingray 1 ($\alpha = -0.87$) being typical for AGN jets, and Stingray 2 ($\alpha = -1.77$) (see Table 2) being typical for a remnant radio galaxy. The spectral index alone is tentative evidence to use to classify the Stingrays, as we are currently unable to resolve any spectral differences between the possible jets/lobes and core.

The most typical morphology that appears similar to the Stingrays is that of an FR II (Fanaroff & Riley 1974) single-jetted AGN with the host galaxy located at the end of the tail. As radio AGN require a host galaxy, we search for possible hosts in the optical and IR regime, specifically DESI DR10 and WISE catalogues, to search for the brightest galaxies within the Stingrays's areas. We primarily searched near the tail structure, as this emission appears most morphologically similar to typical radio AGN jet appearance. We find a potential tail-located candidate for Stingray 1, WISEA J012939.26−535841.0 (Figure 7, top panel, red inset). This galaxy has a redshift of 0.059678± 0.00015 (Loveday et al. 1996), corresponding with a Hubble distance of 261.78±18.35 Mpc. We are able to resolve the galaxy into three distinct components with the high-resolution EMU image (Figure 1, top inset). The galaxy appears to be oriented perpendicular to the tail structure in the optical image (Figure 7), and the three radio components are oriented along the axis of the tail. If this is the host, then the diffuse emission is the jet and lobe structure of an AGN jet originating from this galaxy.
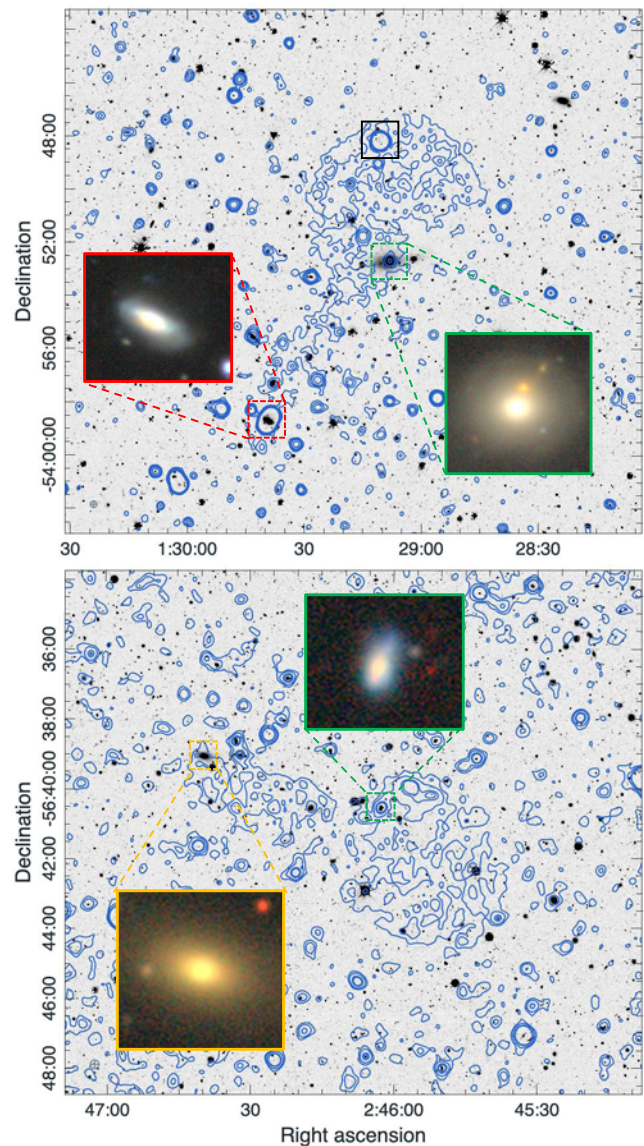
Figure 7. Optical images from the DESI Legacy Survey DR10 overlaid with ASKAP EMU radio contours of Stingray 1 (top) and Stingray 2 (bottom). The optical images are averaged over the g, r, i, and z bands. The radio contours are at levels 60, 120, 200, and 400 μJy beam^{-1} for Stingray 1 and at levels 30, 80, 200, and 250 μJy beam^{-1} for Stingray 2 (right). The red inset shows potential AGN galaxy host WISEA J024639.50−563904.2 for Stingray 1 (top) analysed in Section 4.2.1. The green insets show the coloured DESI DR10 images of the potential central galaxy groups/pairs, LEDA 425198 (top) and of 2dFGRS TGS845Z440 for Stingray 2 (bottom) analysed in Section 4.2.4. The black square (top) shows the location of the galaxy cluster J012910.8−534812 for Stingray 1 and the orange square (bottom) shows the location of the galaxy cluster J024639.5−563904, with the inset showing the coloured DESI DR10 image of the BCG LEDA 398369 analysed in Section 4.2.3.

We also note a potential candidate for Stingray 2, however, it is not located at the tail. The brightest emission section of the northern rim of Stingray 2 in the radio morphology appears to resemble a bent-tail radio galaxy. It is located on the periphery of the structure, although still within the Stingray 2 emission. We observe no optical counterpart in the DESI optical images, and thus no identifiable host galaxy.

A possible concern with the radio AGN scenario is that at these redshifts, the Stingrays would have vastly different physical sizes. Stingray 1 would measure $\sim$1.1 Mpc from head to tip of the tail

while Stingray 2 would measure ∼2.4 Mpc. It is difficult to correlate such similar shapes with such a large difference in physical size unless Stingrays are some form of ORCs (see Section 4.2.6). However, these large sizes may also indicate that they may be similar objects at different ages. If Stingray 2 is older, then this could help to explain the larger size, as well as the lower surface brightness and the steeper spectral index, as the emission has faded and lost its highest energy electrons as it ages.

While it is possible that the Stingrays are FR II single-jetted AGNs, the morphology still raises concerns with this classification. Mainly, there is a sharp disparity between the tail and circular sections, particularly pronounced for Stingray 1. This scenario would require a highly energetic radio jet to abruptly disperse and form an almost perfectly circular radio lobe. This would be an unusual morphology for an AGN, as the lobes typically flare out into more asymmetrical shapes. However, AGNs can display a diverse range of morphologies, and so this scenario is a tentative possibility.

4.2.2. Dying radio galaxy

Another possibility is that the Stingrays are a relic or remnant emission of a dying radio galaxy. This is an evolutionary phase of some radio galaxies, where it is believed that the galactic nuclear activity has ceased, but the remnant radio lobes are still detectable for some time before they disappear completely (Cordey 1987; Komissarov & Gubanov 1994). Due to the cessation of constant energy injection, the lobes are subject to radiative losses of the relativistic electrons, which can result in steep radio spectral indices, $\alpha \lesssim -1.3$ (Komissarov & Gubanov 1994; Dutta et al. 2023). The first relic radio galaxy discovered is IC 2476 by Cordey (1987), and while it is still a relatively sparse population, there are several other examples (Harris et al. 1993; Parma et al. 2007; de Gasperin et al. 2014; Brienza et al. 2016; Duchesne & Johnston-Hollitt 2019; Oozeer et al. 2021)

The morphology of the Stingrays is also not particularly similar to any previously observed for dying radio galaxies, arguing against this scenario. It is also unusual that the morphologies would be so similar, while there is a substantial difference in spectral index. This difference in spectral index indicates that the objects may be of different ages, so it is unusual that radio galaxies at different ages display such similar morphologies. It is difficult to correlate these discrepancies with the scenario of a restarted remnant galaxy, but the morphology alone does not preclude the possibility.

A dying radio galaxy is a more plausible scenario for Stingray 2 compared with Stingray 1 due to the observed spectral indices. The spectral index of Stingray 2 ($\alpha_{Total} = -1.77 \pm 0.06$) (Tables 4 and 2), is within the range for a dying radio galaxy. The morphology of a connected circular and tail region is unusual for a dying radio galaxy, yet there are some that do exhibit unusual morphologies (Harris et al. 1993; de Gasperin et al. 2014). If the Stingrays are relic radio galaxies, then it is likely that the host galaxy is one of those mentioned in Sections 4.2.1 and 4.2.4. In the case of the tail-situated galaxy for Stingray 1, the emission would have formed by a jet forming a circular lobe-like structure, and in the case of the central-situated galaxies, then it may be two jets with vastly different morphologies due to different environments or galactic winds. In the case of Stingray 1, we also have the possibility that the tail may represent a radio bridge connecting the two galaxies. This is a possibility as the tail-situated galaxy (described in Section 4.2.1) and the central-situated galaxy (described in Section 4.2.4) have

similar redshift values and may be located in the same galaxy group.

It has also been observed that dying galaxies can restart (Jones & Preston 2001; Saikia & Jamrozy 2009), and so the dying radio lobe can be associated with spatially separated newly-born jets. Figure 3 shows that the components of Stingray 2 have different spectral indices, indicating that the radio emission may be caused by different physical mechanisms or that they may be similar objects but with different ages. This is consistent with what may be expected from such a restarted source, where we only see one of the restarted jets. However, it is unexpected that the jet would display a steeper spectral index than the dying radio lobe. This is because the jet would have more efficient particle acceleration than the fading lobe, and so would exhibit a flatter spectral index.

4.2.3. Galaxy cluster

Galaxy clusters can generate extended radio emission in the form of radio halos, typically circular emission regions around the cluster centre, and radio relics, elongated shapes at the cluster edges. Both are caused by synchrotron radiation from relativistic electrons, and are typically associated with clusters that display merger activity (van Weeren et al. 2019; Loi et al. 2023; Koribalski et al. 2024b). Radio halos typically have spectral indices $\alpha = -1.2$ to $\alpha = -1.7$, while radio relics have steeper indices up to $\alpha = -2.0$ due to their older electron population (Feretti et al. 2012; van Weeren et al. 2019). Galaxy clusters can have both radio halos and radio relics associated with them (e.g. Pearce et al. 2017; Loi et al. 2023; Velović et al. 2023; Macgregor et al. 2024).

We search several available galaxy cluster catalogues (Planck Collaboration et al. 2016; Gonzalez et al. 2019; Hilton et al. 2021; Bulbul et al. 2024; Thongkham et al. 2024; Wen & Han 2024) and find one catalogued galaxy cluster for each Stingray, both identified in the catalogue of Wen & Han (2024). For Stingray 1, this galaxy cluster is J012910.8−534812, located on the north-western edge of the Stingray 1 emission (see Figure 7). This galaxy cluster has a measured cluster redshift of $z_{phot} = 0.9969$, a radius of 402 kpc, and a mass of 0.56×10^{14}~$M_{\odot}$. At this redshift, Stingray 1's total length would have a physical size of 6.72 Mpc, much larger than the given cluster radius. This size is unrealistically large for such an association, and strongly argues against this scenario for Stingray 1. The cluster has a bright radio counterpart, which appears as a point source with an integrated flux density of 17.6 mJy from the EMU data. It likely corresponds to a known radio galaxy, WISEA J012910.84−534811.7 (also SUMSS J012910−534811) and has a measured SUMSS 843 MHz flux density of $S = 21.6 \pm 1.1$ mJy and a redshift of $z_{phot} = 0.94 \pm 0.06$.

For Stingray 2, the galaxy cluster is J024639.5−563904 located at the tip of the tail section (see Figure 7). Wen & Han (2024) give a redshift of $z_{phot} = 0.2127$, a radius of 773 kpc, and a mass of 1.69×10^{14}~$M_{\odot}$. At the cluster redshift, Stingray 2 would have a total physical length of 2.07 Mpc, almost three times larger than the cluster radius from Wen & Han (2024). The brightest cluster galaxy LEDA 398369 has a redshift of $z_{phot} = 0.222 \pm 0.005$ from the Legacy Survey DR9 dataset. LEDA 398369 may be responsible for the Stingray emission.

Galaxy clusters can have associated diffuse radio emission, for example, halos and/or relics. The clusters identified above are located within the Stingray emission, yet very near the edge in both cases. The diffuse radio emission from the Stingrays also extends much beyond the catalogued cluster radii. For Stingray 1, the emission is approximately 17 times larger than the cluster radius, and

for Stingray 2, it is approximately 2−3 times larger. Galaxy cluster emission typically ranges from a few hundred kpc up to 1−2 Mpc in size (van Weeren et al. 2017). Stingray 1 emission is significantly larger than this range, and Stingray 2 is on the very upper edge. This larger size, combined with the galaxy cluster not being located near the geometric centre of the emission, makes it unlikely that these are hosts for the emission. It is possible that there are non-catalogued galaxy clusters within the emission which may make these larger sizes more realistic. Due to the Stingray's large sizes however, the potentially uncatalogued cluster would have to be relatively nearby. For example, an upper redshift limit of ∼0.3 would give the Stingrays physical sizes of ∼ 3.8 Mpc for Stingray 1 and ∼ 2.7 Mpc for Stingray 2, which are unrealistically large for a galaxy cluster scenario. Therefore, the cluster would need to be $z < 0.3$ as a conservative upper limit, and this would require several tens or hundreds of nearby galaxies to be missing from current catalogues, which is an unlikely scenario.

As both catalogued clusters are on the edge of the emission, if there were another cluster at the other end or more centrally located, then the emission may represent a bridge structure connecting these separate structures. This may help explain the unusual morphology and the larger sizes, however we currently have no direct evidence that there are more clusters located within the emission.

Another caveat to this scenario is that galaxy cluster radio emission is typically accompanied by X-ray emission due to the hot, ionised gas. The area of the Stingrays has only been observed by eROSITA in X-ray, not by the more sensitive *Chandra* or *XMM-Newton* telescopes. We searched in the available eRASS images, and detected no corresponding diffuse X-ray emission for the Stingrays, potentially arguing against this galaxy merger scenario. It is possible, there may be X-ray emission that is below eROSITA's sensitivity limits and would require deeper X-ray observations to be detected.

4.2.4. Galaxy pair/group

There is also the possibility that the radio emission may be being caused by a smaller galaxy group, or an interacting galaxy pair, which is the Brightest Group Galaxy (BGG) for a small galaxy group. We searched the entire emission by eye for optical sources, with a preference for more centrally located sources, which appeared to have a potential interacting companion.

For Stingray 1, a possible host is the early-type galaxy WISEA J012908.17−535241.1 (LEDA 425198), shown in Figure 7 (top panel, green inset) which has a spectroscopic redshift of $z_{spec} = 0.051873 \pm 0.000150$ (Jones et al. 2004, 2009). This would give Stingray 1 a distance of 227.8±16.0 Mpc, a total size of∼0.843 Mpc (the longest axis from the edge of the circular region to the tip of the tail), and a circular size of ∼0.425 Mpc. Just west of LEDA 425198 is a smaller companion galaxy (LEDA 425213) which has a similar redshift of $z_{phot} = 0.066 \pm 0.008$ from the Legacy Survey DR9 (Zhou et al. 2025). The diffuse light surrounding the two galaxies suggest they are an interacting galaxy pair.

While galaxy pairs do not typically generate complex diffuse radio emission, it has recently been observed in the 'Physalis' system (Koribalski et al. 2024c). Such complex emission is also observed in slightly larger galaxy groups such as 'Stephan's Quintet' (Stephan 1877; Xu et al. 2003). To determine if there is a sufficient galaxy density in the area surrounding LEDA 425198 to support a larger group, we sample a 1° region around Stingray 1 using the NED database. We find 69 galaxies with known redshift

values within the region. We take a redshift range which contains LEDA 425198, $0.031873 < z < 0.051873$, and find that 21 of these fall within. Therefore, this galaxy density makes it a possibility that there is a small galaxy group where LEDA 425198 is the BGG.

LEDA 425198 is located in the centre of Stingray 1, between the circular and tail sections with a possible interacting companion, LEDA 425213 (see Figure 7, top panel, green inset). It is possible that the distinct circle and tail sections we see are tidal features caused by this potential interaction. They may be outflows from the elliptical galaxy that show distinctly different shapes due to asymmetric gravitational effects from the interaction. That is, the circular region may be an outflow that is being bent into this circular shape by the gravitational interaction, causing this distinct morphology. A potential issue with this scenario is the large physical size at this redshift. While galaxy clusters can reach up to a few Mpc in some cases, galaxy group or pair emission is typically smaller. For example, the Physalis structure has a physical size of 145×116 kpc (Koribalski et al. 2024c) and Stephan's Quintet has a slightly larger length of ∼0.6 Mpc (Xu et al. 2022). Such a large physical size is unlikely to be caused by a small galaxy group or interacting galaxy pair. Therefore, LEDA 425198 may be a BGG for a group here, however it is difficult to confirm this group membership.

If LEDA 425198 is the host galaxy, then the Stingray 1 emission may be bent remnant lobes from potential interaction with its companion. In this scenario, the remnant or relic lobes originate from previous activity of the currently inactive BGG LEDA 425198, and the resulting lobes are being bent by the surrounding environment, with one being pushed down to form the linear tail-like feature, and the other bending around in an arc to form the circle-like structure.

There is a similar galaxy within Stingray 2 (Figure 7, bottom panel, green inset), WISEA J024602.67−564033.5 (2dFGRS TGS845Z440), that may also have an interacting companion. For the companion, we follow a similar procedure for the Stingray 1 object, searching the Gaia DR3 (Gaia Collaboration et al. 2023), 2MASS (Skrutskie et al. 2006), and allWISE (Cutri et al. 2021) catalogues, however do not find the source listed. Therefore, this may represent a galaxy pair, but this cannot be confirmed with the current data. Following a similar argument, this may be a BGG host for Stingray 2. 2dFGRS TGS845Z440 has a redshift of 0.154600±0.000297, as measured by the 2dF Galaxy Redshift Survey (Colless et al. 2003). At this redshift, Stingray 2 would have a distance of 682.4±47.8 Mpc and a size of ∼1.903 Mpc (the longest axis from the edge of the circular region to the tip of the tail). Using a similar analysis as above, we find 305 galaxies within a 1° diameter. This is a higher galaxy density than for Stingray 1 overall, and the redshift range that 2dFGRS TGS845Z440 is located in, $0.1499 < z < 0.1599$, contains 31 galaxies. Therefore, it is possible that, similar to Stingray 1, there is a small galaxy group with 2dFGRS TGS845Z440 as the BGG.

Since 2dFGRS TGS845Z440 is also located roughly between the circular and tail sections and appears to have an interacting companion, we can make a similar argument as above. It is possible that the tail and circular region are both jets, with one being bent by the gravitational interaction. Stingray 2's physical size is even larger in this scenario, and thus it is equally unlikely that such a large structure could be caused by a a small galaxy group or pair. It is possible that both Stingrays display an interacting galaxy pair at a central location and that the unique morphologies may be the result of an unusual gravitational interaction. The main issue with

this scenario is that it is difficult to explain the large physical sizes, making this explanation unlikely.

4.2.5. Head-tail radio galaxy

Another possibility is that the Stingrays could be head-tail radio galaxies, which are formed by the passage of a strong wind or shock front. This passage suggests blowing back one of the jets and making it almost disappear, which can generate plumes or ring-like structures. The underlying idea is presented in Nolting et al. (2019), and this interpretation was used to explain the unusual structure of the Corkscrew galaxy (Koribalski et al. 2024a). In the case of the Stingrays, this would involve jets originating from the tail-situated potential host galaxy. Head-tail radio galaxies have several predicted morphological characteristics which appear to match both Stingrays, particularly Stingray 1. They predict a one-sided jet ending in a circular structure at the end of the jet, where the wind is blowing the jet back to form a circular plume-like structure. They predict that the head section is slightly separated from the tail section, which matches with the slight brightness dip observed in Stingray 1 where the tail meets the circular region. It also predicts that the host galaxy is slightly offset from the jet origin point, which is observed in Stingray 1, where the obvious radio galaxy WISEA J012939.26−535841.0 (Figure 7, top panel, red inset), is offset slightly to the east from the tail. This scenario plausibly explains all of the unusual morphological characteristics of Stingray 1 and thus presents the most likely scenario out of those discussed.

This scenario is also a possibility for Stingray 2, which displays a similar morphology. The caveat here, however, is that there is no obvious host galaxy for the Stingray 2 emission. There is a prominent radio source, LEDA 398369 (Figure 7, bottom panel, red inset), located at the tail tip for Stingray 2, but this is classified as a cluster and not a single radio galaxy. While head-tail structures such as this are associated with single radio galaxies, it is possible that a similar structure could form from a similar mechanism on a larger scale, explaining Stingray 2's morphology. Conversely, it is possible that there is a similar host galaxy as for Stingray 1, but it has not yet been identified.

4.2.6. ORC

ORCs are a recently discovered class of radio sources whose nature and origin is still under investigation. Three single ORCs are currently known, ORCs 1 and 4 (Norris et al. 2021) and ORC 5 (Koribalski et al. 2021), each centred on a massive elliptical galaxy. They have sizes of ∼1′, or 300–500 kpc at the host galaxy redshift. The ORCs 2+3 pair (Norris et al. 2021b, Macgregor et al. in preparation), consist of a radio ring, without a central galaxy, and a diffuse blob. These are most likely the lobes of a re-started radio galaxy.

The known single ORCs are characterised by their edge-brightened, near-circular radio emission, for which no counterparts have been detected at non-radio wavelengths, and their steep spectral indices. They are often associated with a central host galaxy, and diffuse radio emission. MeerKAT images of ORC 1 also show internal ring structures (Norris et al. 2022). Various formation mechanisms have been suggested (Norris et al. 2021; Koribalski et al. 2021; Dolag et al. 2023; Shabala et al. 2024), but the rarity of ORCs means our knowledge of their properties is still very limited. The search for ORCs is ongoing, and several ORC candidates are discussed in the literature (Gupta et al. 2022; Lochner et al. 2023; Koribalski et al. 2024b, Filipović et al. in preparation;

Macgregor et al. in preparation), as well as possibly related, much closer radio shell systems (Koribalski et al. 2024c).

The two peculiar radio sources discussed in this paper, Stingrays 1 and 2, share some common characteristics with ORCs. Their main body is predominantly circular, somewhat edge-brightened, partially filled with diffuse emission, and have a steep spectral index. However, no central radio source or obvious host galaxy was detected. Furthermore, a distinct, one-sided tail structure is detected, similar in size and surface brightness to the main body. Also, both Stingrays have angular sizes much larger than the currently identified ORCs. Therefore, it is possible that the Stingrays may be a type of ORCs that displays jet-like structures. AGN jets viewed from a specific orientation have been theorised as a potential explanation for ORCs (Norris et al. 2021; Norris et al. 2021b; Lin & Yang 2024; Shabala et al. 2024). The origin of ORCs is still debated in the literature, and jets are not defined as one of the characteristic observable features. Therefore, it would be premature to make this classification without further investigation due to these discrepancies.

It is also possible that the morphology may be more similar to an ORC if viewed from a different orientation. For example, if the host galaxy were at the tip of the jet and the orientation was such that the jet was directed along our line of sight and then expanded out into the circular region, it is possible that the jet would not be visible from this orientation, and instead, the Stingray would resemble a structure where the host galaxy appears to be inside a circle of diffuse emission. In this orientation, the Stingray may appear much more morphologically similar to an ORC.

Another potential possibility is that ORCs have jets when they are younger which fade as they age. Therefore, the population that we have identified thus far no longer has observable jets. In the case of the Stingrays, if the jets were to fade then what would be left behind is a quite circular patch of emission that would not be appear to be associated with a galaxy; a situation which holds true for some ORCs, namely the ORC 2+3 pair (Norris et al. 2021b, Macgregor et al. in preparation). As the true nature and origin of ORCs is still under investigation, these are currently purely speculative scenarios.

4.2.7. Chance alignment

It is also possible that the circular and tail regions of both Stingrays are not physically associated at all, and their unusual morphology is caused by a chance alignment of two or more sources. It should also be noted that both Stingrays display a slight drop in intensity at the region where the circle and tail sections intersect. This might indicate that the emission is not physically associated.

If this scenario is the case, then the objects would consist of a radio tail structure and a circular region. The tail structure would be typical of an unresolved AGN (Section 4.2.1), and the circular region could be a galaxy cluster halo (Section 4.2.3) or an ORC (Section 4.2.6). Stingray 2 displays several optically bright galaxies in the circular region (Figure 7) that may generate enough diffuse radio emission to form this circular halo structure. This scenario is less likely for Stingray 1 as there are far fewer optically bright galaxies present in the circular region.

5. Conclusions

We have conducted a radio analysis of two unusually shaped diffuse radio sources that we named 'Stingrays'. These Stingrays are

diffuse regions of radio emission, characterised by a circular section with a connected tail-like section extending out. There is no corresponding diffuse emission found at any other frequency. We investigate several possible origin scenarios, both Galactic/near Galactic and extragalactic.

We explored several Galactic/near Galactic scenarios:– Runaway SNRs from the MCs: This scenario involves runaway stars from the MCs, which then exploded and formed SNRs within the MS. Our HI analysis shows that the objects are likely not associated with the MS and are in the same line of sight. The measured spectral index values are also not consistent with the MC SNR population. This scenario is deemed unlikely.

– Circumgalactic SNRs: Similar to the runaway SNR scenario, this scenario involves SNRs which formed on the outskirts of the MCs and are located just outside the galaxies themselves. The spectral index values are not consistent with the MC SNR population, and neither are the physical sizes at the MC distances. This scenario is deemed unlikely.

– Parentless PWN: A PWN without an associated SNR. The steep spectral index is at odds with this scenario, and this scenario is deemed unlikely.

We also explored several extragalactic scenarios for the Stingrays.– Radio AGN: This scenario involves powerful jets and lobes from a radio AGN which have formed unusual morphologies, likely through some kind of environmental interaction. This is a more likely scenario for Stingray 1, as a most likely host is identified as WISEA J012939.26-535841.0, located at the tip of the tail. The spectral indices and sizes can be explained in this scenario, and it is deemed a possible scenario for both Stingrays.

– Dying radio galaxy: This scenario involves a radio galaxy where the galactic nuclear activity has ceased, but the remnant radio lobes are still visible. The morphology causes some issues with this scenario, but the spectral indices, particularly for Stingray 2, are consistent. This is deemed a possible scenario for both Stingrays.

– Galaxy cluster: We find a catalogued galaxy cluster located in the emission of each Stingray, and galaxy clusters can display extended radio emission. The clusters are located on the peripheries of both Stingrays and the associated physical sizes are larger than expected for a cluster scenario at the given redshifts. This scenario would be possible if more galaxy clusters are found within the emission in the future. This scenario is currently deemed unlikely for both objects.

– Galaxy pair/group: There are possible interacting galaxy pairs for both Stingrays, and the galaxy density in both areas is sufficient to support a small galaxy group. Galaxy pairs and groups can display extended radio emission, although the physical sizes of the Stingrays are larger than expected from such a system. This scenario is currently deemed unlikely for both objects.

– Head-tail radio galaxy: This scenario involves a head-tail radio galaxy, which are typically formed by strong AGN jets which are pushed back by strong winds or shock fronts, and form round circular structures. Both Stingrays meet the morphological criteria for these objects, and Stingray 1 has a possible host identified. This scenario is deemed likely for Stingray 1 and possible for Stingray 2, with the caveat that the Stingray 2 host would have to be identified.

– ORC: This scenario involves ORCs, which are circular regions of diffuse radio emission, observed exclusively at radio frequencies. These objects typically have central elliptical host galaxies, which are not identified in the Stingrays. Their morphology is also not characteristic of an ORC, primarily as they are not fully circular. This scenario is deemed unlikely for both objects.

– Chance alignment: This scenario suggests that the Stingrays may not be a single structure, but in fact a circular region superimposed with a tail region. Finding two objects with similar morphologies caused by such a superposition would be statistically unlikely, but is possible for either one or both of the objects. This scenario is deemed possible for both objects.

Overall, several of these scenarios could explain the Stingrays unusual shapes, however, further observations would be required to resolve these uncertainties. For example, more sensitive X-ray observations could detect any corresponding diffuse X-ray emission and help determine the physical properties of the emission, while more sensitive radio observations may reveal detectable polarisation to help map any magnetic field properties and variations.

The final conclusion is that Stingrays are diffuse extragalactic non-thermal radio sources, but their exact nature remains unclear. Their unusual morphology could be caused by orientation effects or complex environmental interactions in several of the proposed scenarios. The most likely scenario from the current data is that of head-tail radio galaxies. This scenario is most likely for Stingray 1, and possible for Stingray 2, but the host galaxy for Stingray 2 would need to be identified.

[g]https://ror.org/05qajvd42.

We thank an anonymous referee for their detailed and constructive comments which greatly improved our paper.

References

Abdollahi, S., et al. 2022, 260, 53

Ball, B. D., et al. 2023, MNRAS, 524, 1396

Balzan, J. C. F., Filipović, M. D., Dai, S., Alsaberi, R. Z. E., & Barnes, L. 2022, 367, 61

Bell, A. R. 1978, MNRAS, 182, 147

Blaauw, A. 1961, BAN, 15, 265

Bland-Hawthorn, J., & Putman, M. E. 2001, in Astronomical Society of the Pacific Conference Series, Vol. 240, Gas and Galaxy Evolution, ed. J. E. Hibbard, M. Rupen, & J. H. van Gorkom, 369

Blandford, R., Meier, D., & Readhead, A. 2019, ARA&A, 57, 467

Bozzetto, L. M., et al. 2017, ApJS, 230, 2

Bozzetto, L. M., et al. 2023, MNRAS, 518, 2574

Bridle, A. H., & Perley, R. A. 1984, ARA&A, 22, 319

Brienza, M., et al. 2016, A&A, 585, A29

Brüns, C., et al. 2005, A&AS, 432, 45

Bulbul, E., et al. 2024, 685, A106

Burger-Scheidlin, C., et al. 2024, 684, A150

Calvi, V., Stiavelli, M., Bradley, L., Pizzella, A., & Kim, S. 2014, ApJ, 796, 102

Chandra, V., et al. 2023, ApJ, 956, 110

Gaia Collaboration, et al. 2023, 674, A1

Planck Collaboration, et al. 2016, 594, A27

Colless, M., et al. 2003, arXiv e-prints, astro

Collier, J. D., et al. 2014, 439, 545

Collier, J. D., et al. 2018, 477, 578

Comrie, A., et al. 2021, CARTA: The Cube Analysis and Rendering Tool for Astronomy, Zenodo

Condon, J. 1984, ApJ, 287, 461

Cordes, J. M., Romani, R. W., & Lundgren, S. C. 1993, Natur, 362, 133

Cordey, R. A. 1987, MNRAS, 227, 695

Cotton, W. D., et al. 2024, MNRAS, 529, 2443

Cutri, R. M., et al. 2021, VizieR Online Data Catalog: AllWISE Data Release (Cutri+ 2013), VizieR On-line Data Catalog: II/328. Originally published in: IPAC/Caltech (2013)

Dabhade, P., et al. 2020, 642, A153

de Gasperin, F., et al. 2014, MNRAS, 440, 1542

Dey, A., et al. 2019, AJ, 157, 168

Diana, A., et al. 2022, MNRAS, 511, 5436

Dolag, K., Böss, L. M., Koribalski, B. S., Steinwandel, U. P., & Valentini, M. 2023, ApJ, 945, 74

Duchesne, S. W., & Johnston-Hollitt, M. 2019, PASA, 36, e016

Dutta, S., et al. 2023, ApJ, 944, 176

HI4PI Collaboration, et al. 2016, A&AS, 594, A116

VukotiÀ Filipović, M. D., et al. 2023, 166, 149

Fanaroff, B. L., & Riley, J. M. 1974, MNRAS, 167, 31P

Feretti, L., Giovannini, G., Govoni, F., & Murgia, M. 2012, A&ASr, 20, 54

Filipović, M. D., et al. 2021, 507, 2885

Filipović, M. D., et al. 2022, MNRAS, 512, 265

Filipović, M. D., et al. 2022, MNRAS, 512, 265

Filipović, M. D., et al. 2024, 41, e112

Filipović, M. D., et al. 2025, 42, e104

Filipović, M. D., & Tothill, N. F. H. 2021, Principles of Multimessenger Astronomy, 2514-3433 (IOP Publishing), doi: 10.1088/2514-3433/ac087e

Galvin, T. J., & Filipovic, M. D. 2014, SerAJ, 189, 15

Gonzalez, A. H., et al. 2019, 240, 33

Gupta, N., et al. 2022, PASA, 39, e051

Guzman, J., et al. 2019, ASKAPsoft: ASKAP Science Data Processor Software, ascl:1912.003

Gvaramadze, V. V., Pflamm-Altenburg, J., & Kroupa, P. 2011, A&AS, 525, A17

Hancock, P. J., Murphy, T., Gaensler, B. M., Hopkins, A., & Curran, J. R. 2012, MNRAS, 422, 1812

Hancock, P. J., Trott, C. M., & Hurley-Walker, N. 2018, PASA, 35, e011

Hardcastle, M. J., & Croston, J. H. 2020, NewAR, 88, 101539

Harris, D. E., Stern, C. P., Willis, A. G., & Dewdney, P. E. 1993, AJ, 105, 769

Haynes, M. P. 1979, AJ, 84, 1173

Hilton, M., et al. 2021, 253, 3

Hopkins, A., et al. 2025, 42, e071

Hotan, A. W., et al. 2021, 38, e009

Hurley-Walker, N., et al. 2017, 464, 1146

Hurley-Walker, N., et al. 2019a, PASA, 36, e048

Hurley-Walker, N., et al. 2019b, PASA, 36, e047

Johnston, S., et al. 2008, ExA, 22, 151

Jones, D. H., et al. 2004, MNRAS, 355, 747

Jones, D. H., et al. 2009, MNRAS, 399, 683

Jones, D. L., & Preston, R. A. 2001, AJ, 122, 2940

Komissarov, S. S., & Gubanov, A. G. 1994, A&A, 285, 27

Koribalski, B., Johnston, S., Weisberg, J., & Wilson, W. 1995, ApJ, 441, 756

Koribalski, B. S., et al. 2020, 365, 118

Koribalski, B. S., et al. 2021, MNRAS, 505, L11

Koribalski, B. S., et al. 2024a, 533, 608

Koribalski, B. S., et al. 2024b, 531, 3357

Koribalski, B. S., et al. 2024c, MNRAS, 532, 3682

Kothes, R., Reich, P., Foster, T. J., & Reich, W. 2017, 597, A116

Lazarević, S., et al. 2024a, RNAAS, 8, 107

Lazarević, S., et al. 2024b, PASA, 41, e032

Leahy, D., & Tian, W. 2010, in The Dynamic Interstellar Medium: A Celebration of the Canadian Galactic Plane Survey, Vol. 438, 365

Leahy, D. A., & Tian, W. W. 2012, A&AS, 539, A128

Lin, Y.-H., & Yang, H. Y. K. 2024, 974, 269

Lin, Z., et al. 2023, ApJ, 952, 64

Lochner, M., Rudnick, L., Heywood, I., Knowles, K., & Shabala, S. S. 2023, MNRAS, 520, 1439

Loi, F., et al. 2023, A&AS, 672, A28

Loveday, J., Peterson, B. A., Maddox, S. J., & Efstathiou, G. 1996, 107, 201

Lucchini, S., D'Onghia, E., & Fox, A. J. 2021, ApJL, 921, L36

Lucchini, S., D'Onghia, E., & Fox, A. J. 2024, ApJ, 967, 16

Macgregor, P. J., et al. 2024, 41, e050

Maggi, P., et al. 2019, A&AS, 631, A127

Mauch, T., et al. 2003, MNRAS, 342, 1117

Meyer, D. M.-A., Langer, N., Mackey, J., Velázquez, P. F., & Gusdorf, A. 2015, MNRAS, 450, 3080

Murgia, M., et al. 2011, A&AS, 526, A148

Nolting, C., Jones, T. W., O'Neill, B. J., & Mendygral, P. J. 2019, 876, 154

Norris, R. P., et al. 2011, PASA, 28, 215

Norris, R. P., et al. 2021a, PASA, 38, e046

Norris, R. P., et al. 2021b, PASA, 38, e003

Norris, R. P., et al. 2022, MNRAS, 513, 1300

Norris, R. P., Crawford, E., & Macgregor, P. 2021, Galaxies, 9, doi: 10.3390/galaxies9040083

O'Dea, C. P., & Owen, F. N. 1986, ApJ, 301, 841

Oozeer, N., et al. 2021, Galaxies, 9, doi: 10.3390/galaxies9040102

Owen, F. N., O'Dea, C. P., Inoue, M., & Eilek, J. A. 1985, ApJl, 294, L85

Parma, P., et al. 2007, A&A, 470, 875

Pavan, L., et al. 2014, A&AS, 562, A122

Pavan, L., et al. 2016, A&AS, 591, A91

Pearce, C. J. J., et al. 2017, ApJ, 845, 81

Pedlar, A., et al. 1990, MNRAS, 246, 477

Pennock, C. M., et al. 2021, MNRAS, 506, 3540

Putman, M. E. 2000, PASA, 17, 1–5

Putman, M. E., Staveley-Smith, L., Freeman, K. C., Gibson, B. K., & Barnes, D. G. 2003, ApJ, 586, 170

Ranasinghe, S., & Leahy, D. 2023, 265, 53

Saikia, D. J., & Jamrozy, M. 2009, BASI, 37, 63

Sasaki, M., et al. 2025, 693, L15

Sault, R. J., Teuben, P. J., & Wright, M. C. H. 1995, in Astronomical Society of the Pacific Conference Series, Vol. 77, Astronomical Data Analysis Software and Systems IV, ed. R. A. Shaw, H. E. Payne, & J. J. E. Hayes, 433

Shabala, S. S., et al. 2024, PASA, 41, e024

Shobhana, D., et al. 2023, 519, 4902

Skrutskie, M. F., et al. 2006, 131, 1163

Smeaton, Z. J., et al. 2024a, RNAAS, 8, 158

Smeaton, Z. J., et al. 2024b, MNRAS, 534, 2918

Smeaton, Z. J., et al. 2025, SerAJ, 210, 13

Stephan, M. 1877, 37, 334

Theil, H. 1950, IM, 12, 173

Thongkham, K., et al. 2024, 967, 123

van Weeren, R. J., et al. 2017, ApJ, 835, 197

van Weeren, R. J., et al. 2019, SSR, 215, 16

Velázquez, P. F., Vigh, C. D., Reynoso, E. M., Gómez, D. O., & Schneiter, E. M. 2006, ApJ, 649, 779

Velović, V., et al. 2022, MNRAS, 516, 1865

Velović, V., et al. 2023, MNRAS, 523, 1933

Virtanen, P., et al. 2020, NM, 17, 261

Wang, J., Hammer, F., & Yang, Y. 2022, MNRAS, 515, 940

Wayth, R. B., et al. 2015, PASA, 32, e025

Wen, Z. L., & Han, J. L. 2024, 272, 39

Wenger, M., et al. 2000, A&ASs, 143, 9

Westmeier, T., et al. 2022, 39, e058

Xu, C. K., et al. 2022, Natur, 610, 461

Xu, C. K., Lu, N., Condon, J. J., Dopita, M., & Tuffs, R. J. 2003, 595, 665

Yew, M., et al. 2021, MNRAS, 500, 2336

Zangrandi, F., et al. 2024, 692, A237

Zhang, B., et al. 2021, MNRAS, 503, 5385

Zhou, X., et al. 2025, 536, 2260
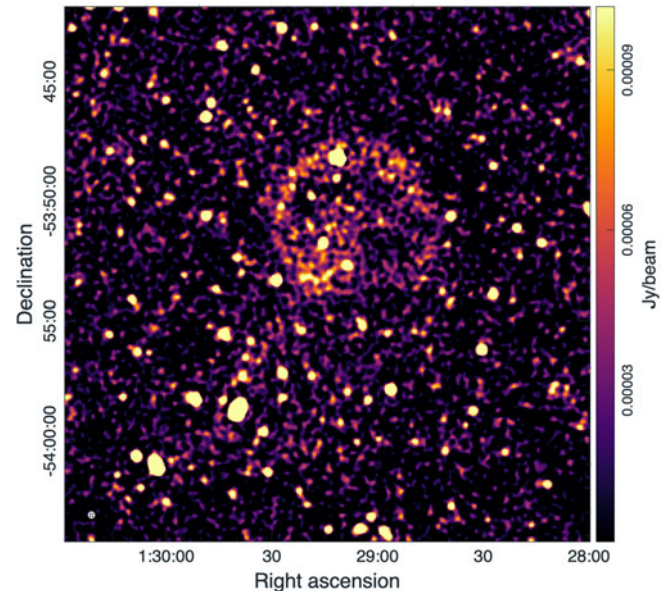
Appendix: WALLABY radio continuum image

Figure A1. ASKAP WALLABY 1.4 GHz radio continuum image of Stingray 1. The image has linear scaling and has been convolved to 15″ resolution, indicated in the bottom left corner. We measure an Root Mean Squared RMS noise sensitivity of $\sigma \sim$25–30 μJy beam^{-1} near Stingray 1.